Subconductance States of Cx30 Gap Junction Channels: Data from Transfected HeLa Cells versus Data from a Mathematical Model

Rolf Vogel,* Virginijus Valiunas,[†] and Robert Weingart[†]

*Department of Cardiology, University Hospital Bern, Bern, Switzerland; and [†]Institute of Physiology, University of Bern, Bern, Switzerland

ABSTRACT   Human HeLa cells expressing mouse connexin30 were used to study the electrical properties of gap junction channel substates. Experiments were performed on cell pairs using a dual voltage-clamp method. Single-channel currents revealed discrete levels attributable to a main state, a residual state, and five substates interposed, suggesting the operation of six subgates provided by the six connexins of a gap junction hemichannel. Substate conductances, $\gamma_{j,substate}$, were unevenly distributed between the main-state and the residual-state conductance ($\gamma_{j,main\ state} = 141$ pS, $\gamma_{j,residual\ state} = 21$ pS). Activation of the first subgate reduced the channel conductance by $\sim$30%, and activation of subsequent subgates resulted in conductance decrements of 10–15% each. Current transitions between the states were fast ($<$2 ms). Substate events were usually demarcated by transitions from and back to the main state; transitions among substates were rare. Hence, subgates are recruited simultaneously rather than sequentially. The incidence of substate events was larger at larger gradients of V_j. Frequency and duration of substate events increased with increasing number of synchronously activated subgates. Our mathematical model, which describes the operation of gap junction channels, was expanded to include channel substates. Based on the established V_j-sensitivity of $\gamma_{j,main\ state}$ and $\gamma_{j,residual\ state}$, the simulation yielded unique functions $\gamma_{j,substate} = f(V_j)$ for each substate. Hence, the spacing of subconductance levels between the channel main state and residual state were uneven and characteristic for each V_j.

INTRODUCTION

Gap junctions establish functional cell-to-cell contacts in most tissues of vertebrates. They mediate the exchange of signaling molecules and ions between neighboring cells and thus provide a means to coordinate the functional state of the cells in tissues. Gap junctions constitute assemblies of tightly packed intercellular channels. Each channel consists of two hemichannels (connexons) embedded into the membranes of adjacent cells. Each hemichannel contains six integral membrane proteins (connexins), which form a hexagon with a central aqueous pore (1). So far, at least 19 different connexins have been identified in vertebrate tissues encoded by a multigene family (2). It is generally assumed that all connexins exhibit the same membrane topology. Hence, it is reasonable to postulate that each connexin participates equally in the channel properties. With regard to the voltage gating between the main and residual states, each connexin is expected to possess a subgate, i.e., a molecular domain governed by the transjunctional voltage, which contributes to the channel subconductances.

Subconductance events have been observed sporadically in vertebrate gap junctions consisting of connexins (3–11) and invertebrate gap junctions made of innexins (12–15). More recently, substates have also been identified in gap junction hemichannels (16,17). Few investigators have attempted to quantitatively study these states studying vertebrate (7,18) and invertebrate cells (13,15). It turned out that the incidence of substates was rather low, thus hampering systematic studies.

We have previously examined the electrical properties of connexin30 (Cx30) gap junction channels of vertebrates (17,19). These studies consistently showed that subconductance states frequently occur at the beginning of pulses with large transjunctional voltage gradients or during sustained pulses with small to intermediate gradients. In addition, the considerable high channel conductance, i.e., about 180 pS (19), allows us to resolve substate events. Hence, Cx30 channels seemed nicely suited for quantitative studies of subgate properties. Using stably transfected human HeLa cells expressing mouse Cx30, we have performed electrophysiological measurements on cell pair preparations in conjunction with the dual voltage-clamp method. To elucidate the results obtained from these studies, we have modified our mathematical gap junction model (20,21) by including channel substates. Preliminary reports have been published before (22,23).

METHODS

Cells and culture conditions

Experiments were carried out on human HeLa cells stably transfected with mouse DNA coding for connexin30 (19,24). The cells were grown in Dulbecco's medium (DMEM) containing 10% FCS, 100 μg/ml streptomycin, and 100 U/ml penicillin (code 2212, Seromed, Fakola, Basel, Switzerland). To perform experiments, the cells were harvested, resuspended in DMEM

with 10% FCS ($\sim$0.2–1 $\times$ 10^6 cells/ml), and seeded onto sterile glass coverslips placed in multiwell culture dishes ($\sim$10^4 cells/cm^2).

Solutions

Experiments were performed in modified Krebs-Ringer solution (in mM): 140 NaCl, 4 KCl, 2 CaCl$_2$, 1 MgCl$_2$, 5 glucose, 2 pyruvate, and 5 HEPES (pH 7.4). The patch pipettes were filled with pipette solution (in mM): 120 potassium aspartate, 10 NaCl, 3 MgATP, 1 MgCl$_2$, 1 CaCl$_2$, 10 EGTA (pCa $\sim$ 8), and 5 HEPES (pH 7.2). SKF-525A hydrochloride (390 mol wt; Proadifen) was purchased from Biomed Research Laboratories (Plymouth, PA).

Electrical measurements

Electrical measurements were carried out 1–3 days after plating. Glass coverslips with adherent cells were transferred to the experimental chamber mounted on the stage of an inverted microscope (Diaphot-TMD, Nikon; Nippon Kogaku, Tokyo, Japan) superfused with Krebs-Ringer solution at 20–23°C. A horizontal puller (DMZ-Universal; Zeitz-Instrumente, Augsburg, Germany) was used to make patch pipettes from glass capillaries (GC150F-10, Harvard Apparatus, Edenbridge, UK); the filled pipettes had DC resistances of 3–5 MΩ. All experiments were carried out on cell pairs. A dual voltage-clamp method and whole-cell recording were used to control the membrane potentials of both cells and to measure the currents (19).

Voltage and current signals were recorded on chart paper (Gould RS 3400; Gould Instruments, Minneapolis, MN) and videotape (Neurocorder DR-886, Neuro Data Instruments, New York, NY). For off-line analysis, the current signals were filtered at 1 kHz (8-pole Bessel, -3 dB) and digitized at 5 kHz with a 12-bit A/D converter (IDA 12120, INDEC Systems, Capitola, CA). This resulted in a signal-amplitude resolution of about 0.05 pA and a signal-time resolution of 1–2 ms, depending on the noise level. Data acquisition and analysis was done with commercial (C-Lab, INDEC Systems) and custom-made software (25). Single channels were evaluated visually by alignment of the cursor markers on the signal trace. Manually positioned cursors yielded interpolated current levels, differences between current levels, and duration of selected current episodes. For some records, mean current levels were obtained from all point analysis. Curve fitting and statistical analysis were done with SigmaPlot and SigmaStat, respectively (Jandel Scientific, Erkrath, Germany). Unless stated otherwise, the data are expressed as means $\pm$ 1 SE.

Mathematical model

All calculations were performed on a personal computer using MATLAB Version 5.3.1 (R11.1) (The MathWorks, Natick, MA). Our generalized model (20,21) describing the conductive properties of gap junction channels and gap junctions has been modified to perform computer simulations on single-channel substates (Fig. 1). The generalized channel model used voltage-sensitive gating between the main and residual states. Depending on the polarity of the transjunctional voltage, one of the two hemichannels toggles instantly between its high and low conductive states whereas the other hemichannel dwells in the high conductive state. This behavior was adopted to model the single-channel substates, i.e., each single-channel substate reflects the activation or closure of a number of subgates of one hemichannel while the subgates of the other hemichannel are inactivated or open. We introduced the following notation. The number of activated subgates reflects the substate number of the single channel. The single-channel main state and residual state are specified as substates 0 and 6, respectively.

Two essentially different approaches will be presented. The first approach assumes that the connexins Cx$_s$ (s indicates connexin number: $1 \leq s \leq 6$) of a hemichannel cx$_r$ (r indicates hemichannel number: $r = 1, 2$)

represent functionally independent subunits. Thus, the hemichannel conductance is assigned to six identical subunits connected in parallel (Fig. 1 A). Each subunit owns a high (H) and a low (L) conductance state represented by the conductances γ_{Hrs} and γ_{Lrs}, where r and s indicate hemichannel and connexin number, respectively. The toggling between the subunit states is instant. In accordance with the generalized model (20,21), subunit conductances, independent of the state, are governed by the voltage across the respective hemichannel and follow an exponential relationship. Assuming a transjunctional voltage polarity that allows subgating of cx$_2$ (Eq. 2, Fig. 1 A), the model can be described by the following equations:

$$\gamma_1 = \Gamma_H \times e^{V_{j1}/V_H}; \tag{1}$$

$$\gamma_2 = \frac{(6-n) \times \Gamma_H}{6} \times e^{V_{j2}/V_H} + \frac{(n) \times \Gamma_L}{6} \times e^{V_{j2}/V_L}, \, 0 \leq n \leq 6, \tag{2}$$

where γ_1 and γ_2 indicate the conductance of and V_{j1} and V_{j2} the voltage drop across cx$_1$ and cx$_2$. The parameters Γ_H, V_H, Γ_L, and V_L represent constant multipliers and decay rates of single-channel conductance states H and L, respectively, and are calculated from main- and residual-state data, as previously outlined (20,21). Parameter n reflects the substate number, i.e., it indicates the number of activated subgates (i.e., subunit state L), whereas $6 - n$ subgates are inactivated (i.e., subunit state H).

The second approach assumes that the connexins of the gating hemichannel are working in a dependent manner (Fig. 1 B). Thus, each hemichannel is modeled by seven different conductive substates, i.e., the channel main state (no subgate activated, $n = 0$), the channel residual state (all subgates of a hemichannel activated, $n = 6$), and five interposed conductance states. Again, the gating between these seven substates is instant. The conductance of each substate is represented by an exponential conductance-voltage relationship (Eq. 4). The fitting parameters of each state have to be calculated individually. Assuming a transjunctional voltage polarity that allows subgating of cx$_2$ (Fig. 1 B), the model can be described as follows:

$$\gamma_1 = \Gamma_H \times e^{V_{j1}/V_H}; \tag{3}$$

$$\gamma_2 = \Gamma_{subn} \times e^{V_{j2}/V_{subn}}, \, 0 \leq n \leq 6, \tag{4}$$

where γ_1 and γ_2 indicate the conductance of and V_{j1} and V_{j2} the voltage drop across cx$_1$ and cx$_2$. The parameters Γ_{subn} and V_{subn} refer to the constant multiplier and the decay rate of the conductance function from hemichannel cx$_2$ dwelling in the nth substate. For states 0 and 6, Γ_{subn} and V_{subn} correspond to Γ_H, V_H, Γ_L, and V_L, respectively, and can be derived from the main- and the residual-state conductances, as outlined above.

RESULTS

Single-channel conductances

To study single-channel currents, I_j, we selected cell pairs with one or two operational gap junction channels. This requirement was met in weakly coupled cell pairs or normally coupled pairs after far-advanced spontaneous uncoupling (27 cell pairs). In some cases, 75 μM SKF-525A (26) was administered to normally coupled preparations to reduce I_j and hence resolve single-channel events (six cell pairs). As previously shown, this intervention does not affect the conductance of gap junction channels (8,19). Associated with transjunctional voltages, V_j, of intermediate size, we observed current signals with discrete levels interposed between $I_{j,main\ state}$ and $I_{j,residual\ state}$, i.e., the main-state current through the fully open channels (all subgates

A

B

$$\gamma_{\text{Hrs}} = \left(\Gamma_{\text{H}}/6\right) \times e^{V_{\text{jr}}/V_{\text{H}}}$$
$$\gamma_{\text{Lrs}} = \left(\Gamma_{\text{L}}/6\right) \times e^{V_{\text{jr}}/V_{\text{L}}}$$

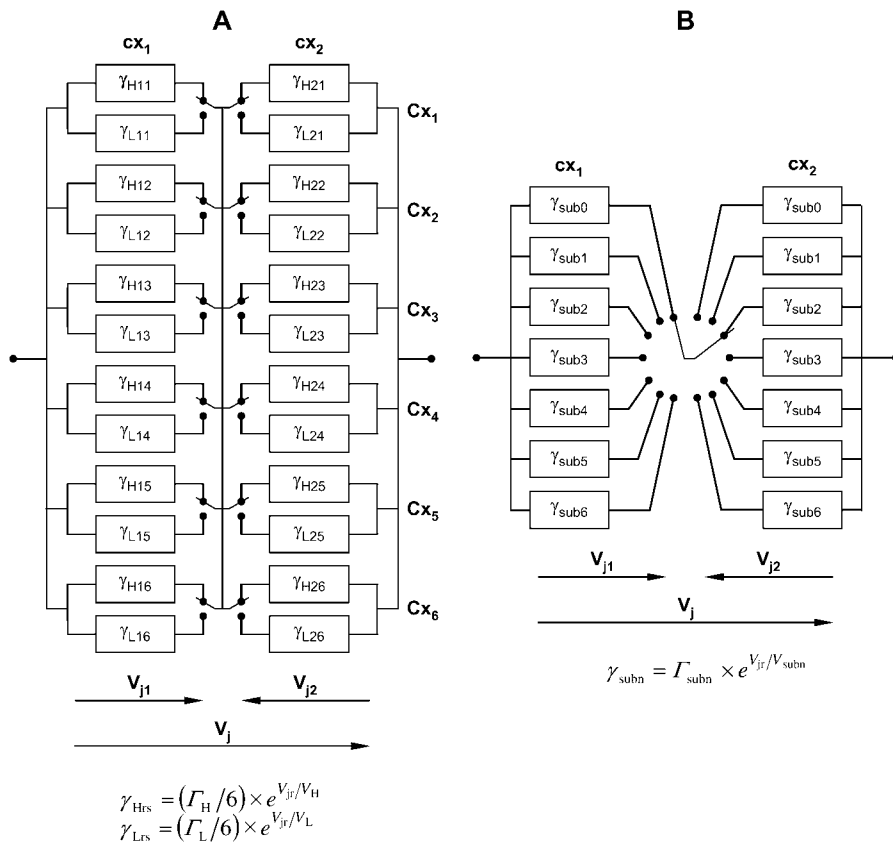$$\gamma_{\text{subn}} = \Gamma_{\text{subn}} \times e^{V_{\text{jr}}/V_{\text{subn}}}$$

FIGURE 1 Electrical schemes representing a single channel and its substates. (*A*) Connexins (Cx) are assumed to work independently; γ_{Hrs} and γ_{Lrs} correspond to the high and low conductive states of connexin s ($1 \leq s \leq 6$) of hemichannel r governed by the hemichannel voltage V_{jr} ($r = 1, 2$). The channel main state is modeled by shifting all switches into the upper position, the residual state by moving either the left or right six switches into the lower position. (*B*) Connexins are assumed to work dependently. Single-channel substates are modeled by seven hemichannel substates. The fitting parameters of each substate (*sub0–sub6*) have to be calculated individually. The main state of the channel is modeled by the conductances γ_{sub0} and γ_{sub0} for hemichannels cx_1 and cx_2, the residual state by γ_{sub0} and γ_{sub6}, respectively.

inactivated) and the residual-state current through the channel with all subgates activated.

Fig. 2 *A* shows current records gained from a weakly coupled cell pair. A hyperpolarizing voltage pulse (duration 200 ms) was administered repetitively (frequency 1 Hz) to cell 2 (V_2) to establish a V_{j} of 75 and 100 mV, respectively. This provoked I_1 signals with rapid transitions giving rise to several discrete current levels. The largest and smallest levels are attributable to $I_{\text{j,main state}}$ and $I_{\text{j,residual state}}$ (*long-dashed lines*), respectively. Since the preparation comprised only one operational channel, the extra current levels (*short-dashed lines*) reflect channel substates, i.e., $I_{\text{j,substate}}$. Fig. 2 *B* shows a single-channel record elicited by a V_{j} of 50 mV amplitude and 3 s duration. It also exhibited current levels ascribable to $I_{\text{j,main}}$, $I_{\text{j,residual}}$, and $I_{\text{j,substate}}$. The inset repeats a segment of the current trace at expanded timescale. It documents at least four resolvable substate events (*short-dashed lines*). Between the first and second substate, an additional event was discernible (*no short dashes*). However, because of the unfavorable current noise, it was excluded from the analysis. Assuming $I_1 = I_{\text{j}} = 0$ pA for $V_{\text{j}} = 0$, the analysis of the current records in Fig. 2 *A* yielded the following conductances, $\gamma_{\text{j,substate}}$: 61 pS (*upper trace*; $V_{\text{j}} = 75$ mV), 44 pS (*lower trace*; $V_{\text{j}} = 100$ mV). For comparison, the values of $\gamma_{\text{j,main state}}$ and $\gamma_{\text{j,residual state}}$ were 147 and 22 pS (*upper trace*) and 137 and 20 pS (*lower trace*), respectively. The current trace in Fig. 2 *B* revealed a $\gamma_{\text{j,main state}}$ and

$\gamma_{\text{j,residual state}}$ of 142 and 23 pS, respectively, and a $\gamma_{\text{j,substate}}$ of 62, 83, 103, and 84 pS (from left to right). The transitions between the main state, substates, and residual state were fast, i.e., they were faster than the frequency response of the recording equipment (<1–2 ms). The lifetime of substates was considerably shorter than that of the main or residual state.

The properties of channel substates were examined systematically by means of two different pulse protocols using short V_{j} pulses (duration 200 ms) with varying amplitude (50, 75, and 100 mV) and long V_{j} pulses (duration >1 s) with fixed amplitude (50 mV). The I_{j} records obtained were assayed for discrete current levels associated with fast transitions. To emphasize the changes in channel conductance, the amplitudes of the current steps were determined using $I_{\text{j,main state}}$ as reference level, i.e., $\Delta I_{\text{j}} = I_{\text{j,main state}} - I_{\text{j,substate}}$. The histogram in Fig. 3 *A* summarizes the data gained at $V_{\text{j}} = 50$ mV (five cell pairs).

The data gathered during long and short V_{j} pulses were not distinguishable and hence were pooled. The conductance changes calculated from the current steps were sampled in 3-pS bins and plotted as number of events versus conductance steps, $\Delta \gamma_{\text{j}} = \Delta I_{\text{j}}/V_{\text{j}}$. The resulting frequency distribution was continuous and broad. Individual conductance steps ranged from 39 to 130 pS. The data were analyzed using an analytical approach (27). The smooth curve corresponds to the best fit of a weighted sum of six Gaussians to the data
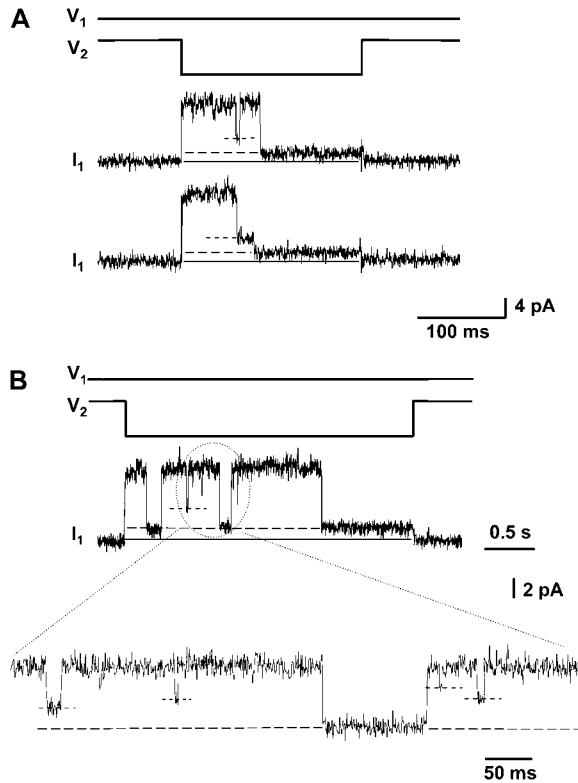
FIGURE 2   Single-channel currents exhibiting subconductance states. (*A*) Application of a voltage pulse to cell 2 (V_2) at maintained voltage of cell 1 (V_1) established a transjunctional voltage, V_j. Current records from cell 1 (I_1) showed discrete levels corresponding to the main state, the residual state (*long dashes*), and a substate (*short dashes*) of a gap junction channel. I_1 signals were obtained from a cell pair with a single gap junction channel. (*Upper trace* ($V_j = 75$ mV)) $\gamma_{j,\text{main state}} = 147$ pS; $\gamma_{j,\text{substate}} = 61$ pS; and $\gamma_{j,\text{residual state}} = 22$ pS. (*Lower trace* ($V_j = 100$ mV)) $\gamma_{j,\text{main state}} = 137$ pS; $\gamma_{j,\text{substate}} = 44$ pS; $\gamma_{j,\text{residual state}} = 20$ pS. (*B*) Current record elicited by a V_j of 50 mV and 3 s: $\gamma_{j,\text{main state}} = 142$ pS, $\gamma_{j,\text{residual state}} = 23$ pS. The inset at an expanded timescale shows four discernible substate events, $\gamma_{j,\text{substate}} = 62$, 83, 103, and 84 pS (*short dashes, left to right*).

using the following values (conductance step and relative frequency): 43 ± 1.6 pS (4%), 56 ± 2.8 pS (5%), 70 ± 4.0 pS (14%), 82 ± 3.0 pS (16%), 98 ± 5.1 pS (21%), and 119 pS ± 3.1 (40%). The most prominent peak was associated with the largest conductance step. The peak related to the smallest conductance step was much smaller.

Fig. 3 *B* shows a histogram of subconductance data gathered at $V_j = 75$ mV (six cell pairs). The spectrum resembles that in Fig. 3 *A*, i.e., it exhibits six discrete conductance peaks with the largest conductance step being the most frequent event. The smooth curve reflects the best fit of a sum of six Gaussians to the data. The analysis yielded the following values (conductance step and relative frequency): 42 ± 7.0 pS (3%), 53 ± 3.8 pS (7%), 68 ± 3.0 pS (15%), 86 ± 6.3 pS (25%), 103 ± 4.6 pS (18%), and 120 ± 3.5 pS (32%).

The data presented in Fig. 3 were then used to determine the relationship between the conductance steps, $\Delta\gamma_j$, and the functional state of the channels. For this purpose, the mean
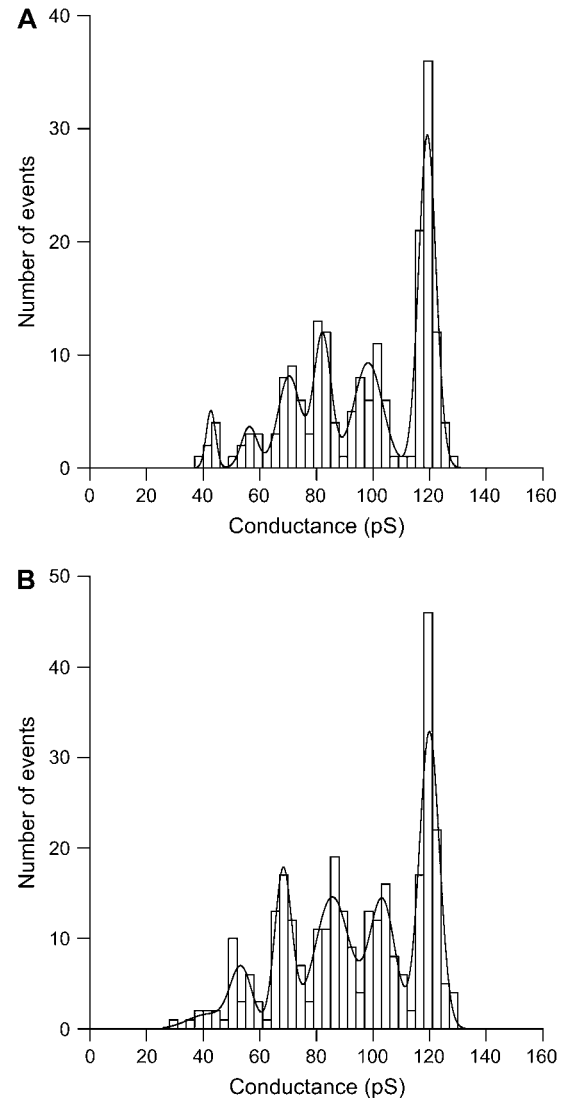
FIGURE 3   Histograms of substate conductances. Conductance steps $\Delta\gamma_j = (\gamma_{j,\text{main state}} - \gamma_{j,\text{substate}})$ obtained from single-channel current records were pooled in consecutive 3-pS bins. The number of observations was plotted as a function of $\Delta\gamma_j$. The distribution was fitted to the weighted sum of six Gauss functions (*continuous curve*). (*A*) Analysis in the case of $V_j = 50$ mV yielded the following mean conductance values (five cell pairs): 43 ± 1.6, 56 ± 2.8, 70 ± 4.0, 82 ± 3.0, 98 ± 5.1, and 119 ± 3.1 pS. (*B*) Analysis in the case of $V_j = 75$ mV (six cell pairs): 42 ± 7.0, 53 ± 3.8, 68 ± 3.0, 86 ± 6.3, 103 ± 4.6, and 120 ± 3.5 pS.

conductance values derived from the binomial distributions were replotted as a function of the assumed number of activated subgates, *n*. Fig. 4 shows the resulting graph. It includes measurements gained at $V_j = 50$ mV (*solid circles*) and 75 mV (*open circles*). No subgate activated ($n = 0$) corresponds to the channel main state indicating the fully open channel; six subgates activated ($n = 6$) corresponds to the channel residual state reflecting the best possible channel closure, i.e., the ground state of V_j-sensitive gating (7,8). The plots of both data sets show a positive correlation between $\Delta\gamma_j$ and *n* and are nearly superimposable. The slight curvature of
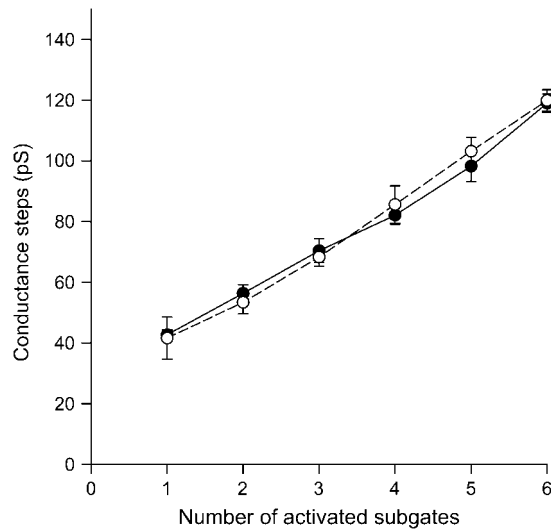
FIGURE 4 Relationship between channel conductance steps and number of subgates activated. Mean conductance values obtained from the analysis of binomial distributions were replotted as conductance steps, $\Delta\gamma_j$, versus number of subgates activated, n; $n = 0$ corresponds to the channel main state, $n = 6$ to the residual state. Symbols correspond to mean values $\pm$ 1 SE. Data represented by solid circles (*continuous line*) and open circles (*dashed line*) were obtained at $V_j = 50$ and 75 mV, respectively.

the graphs indicates that $\Delta\gamma_j$ increased with increasing n. For example, the step from $n = 1$ to $n = 2$ was associated with a conductance change of 13 and 11 pS, whereas the step from $n = 5$ to $n = 6$ was accompanied by a change of 21 and 17 pS for $V_j = 50$ and 75 mV, respectively.

Single-channel conductance profile

The data shown in Fig. 4 were then used to determine the conductance profile of a gap junction channel by subtracting the conductance steps, $\Delta\gamma_j$, from the main-state conductance to obtain the channel conductance levels, $\gamma_j = \gamma_{j,main\ state} - \Delta\gamma_j$. The resulting values were plotted as a function of the number of activated subgates, as shown in Fig. 5. The symbols refer to the mean values at $V_j = 50$ mV (*solid circles*) and $V_j = 75$ mV (*open circle*). The graph indicates that the channel conductance does not decrease linearly with anincreasing number of activated subgates. The activation of the first subgate produced a decrease in conductance considerably larger than the activation of subsequent subgates. The first subgate gave rise to a decrease from 142 to 99 ($V_j = 50$ mV) and from 137 to 95 pS ($V_j = 75$ mV), corresponding to a change of 30% each, whereas subsequent subgate activation produced changes equivalent to 8–15%. As for the single channel, the hemichannel conductance of any substate is larger at the smaller V_j (compare Figs. 5 and 6).

Calculated hemichannel conductance profile

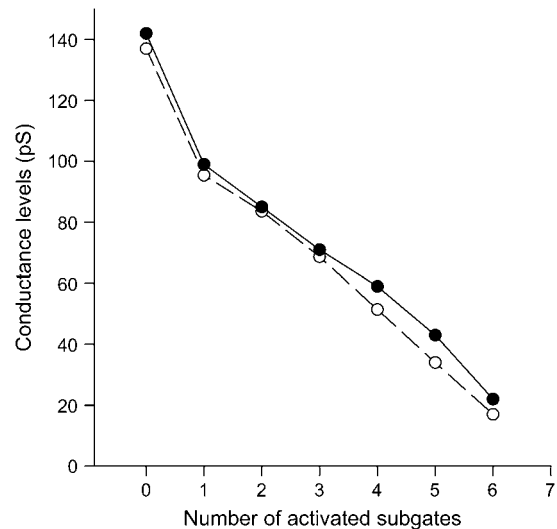Voltage gating of a homomeric-homotypic gap junction channel involves the transition from the high state of one

FIGURE 5 Relationship between channel conductance levels and number of subgates activated. Levels of channel conductance, γ_j, were deduced from the conductance steps, $\Delta\gamma_j$, depicted in Fig. 4 and $\gamma_{j,main\ state}$ according to $\gamma_j = (\gamma_{j,main\ state} - \Delta\gamma_j)$. Values of γ_j were averaged and plotted as a function of the number of subgates activated, n. The conductance at $n = 0$ and $n = 6$ corresponds to $\gamma_{j,main\ state}$ and $\gamma_{j,residual\ state}$, respectively. The data represented by solid circles (*continuous line*) and open circles (*dashed line*) were obtained at $V_j = 50$ and 75 mV, respectively.

hemichannel to the low state or a substate via activation of its subgates while the other hemichannel remains in the high state. Since gap junction channels consist of two hemichannels or connexons arranged in series, i.e., cx_1 and cx_2, their conductance can be expressed as:

$$\gamma_j = (\gamma_{j(cx_1)} \times \gamma_{j(cx_2)})/(\gamma_{j(cx_1)} + \gamma_{j(cx_2)}). \quad (5)$$

This equation allows one to deduce hemichannel conductances during the activation of subgates, γ_{cx}, considering the values for $\gamma_{j,main\ state}$, $\gamma_{j,substate}$, and $\gamma_{j,residual\ state}$. Fig. 6 illustrates the plots of γ_{cx} versus the number of activated subgates at $V_j = 50$ (*solid circles*) and 75 mV (*open circles*) derived from gap junction channel data (see Single-channel conductance profile). Both plots show large changes from $n = 0$ to $n = 1$ and small changes between $n = 1$ and $n = 6$, giving rise to a sharp bend at $n = 1$. Activation of the first subgate reduced the hemichannel conductance from 284 to 152 pS ($V_j = 50$ mV) and from 274 to 145 pS ($V_j = 75$ mV), respectively, corresponding to a decrease of 47% each. In contrast, activation of further subgates led to decreases of 7–11%. This indicates that the activation of the first subgate changes the hemichanel conductance substantially more than the recruitment of further subgates.

Recruitment of substate events

Close examination of the time domain of current records revealed a characteristic pattern of channel substate recruitment. Substate activation and inactivation followed the same
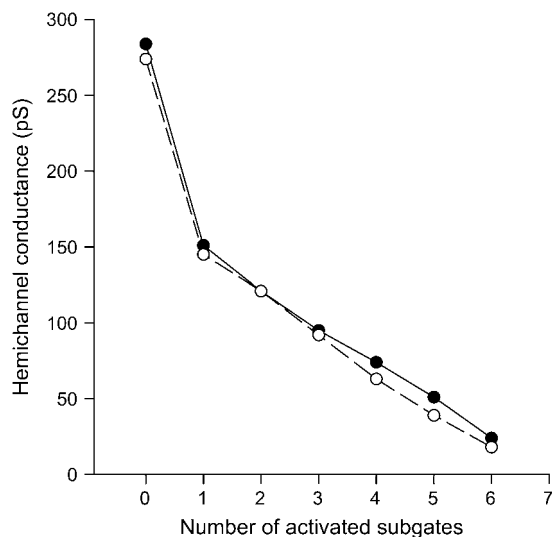
FIGURE 6 Relationship between hemichannel conductance levels and number of subgates activated. Data of channel subconductance levels were used to calculate the conductances experienced by the gated hemichannel of a gap junction channel by means of Eq. 5. The hemichannel subconductances, $\gamma_{j,substate}$, were plotted as a function of the number of subgates activated, n. The data represented by solid circles (*continuous line*) and open circles (*dashed line*) were obtained at $V_j = 50$ and 75 mV, respectively.

general mode. Irrespective of the substate level reached, substates were usually initiated and terminated by fast current transitions from and back to the channel main state. The incidence of transitions between substates and the residual state was only 2–3%; the incidence of transitions among substates was even smaller.

As already shown (see Single-channel conductance profile), the analysis of I_j signals provides information on the incidence of substates. These data can be further analyzed to assess the frequency of channel substate events. For this purpose, the occurrence at each substate level was normalized with the substate exhibiting the highest incidence, i.e., $n = 6$. The bar graphs in Fig. 7 illustrate the normalized frequency of substate events associated with the number of simultaneously activated subgates. For both conditions, i.e., $V_j = 50$ mV (Fig. 7 *A*) and $V_j = 75$ mV (Fig. 7 *B*), the incidence of substate events increased with the number of activated subgates. The frequency distribution of the two data sets did not differ substantially. Interestingly, the absolute number of events observed was smaller at $V_j = 50$ mV (188 events from 235 pulses, i.e., 0.8 events/pulse) than at $V_j = 75$ mV (301 events from 158 pulses, i.e., 1.9 events/pulse).

Dwell times of substates

Current records with a single operational gap junction channel were also used to explore the dwell times at particular substate levels. To this end, we have analyzed the traces elicited by V_j pulses of 200 ms duration. The life times of channel substates were determined for each current trace. Fig. 8 shows the
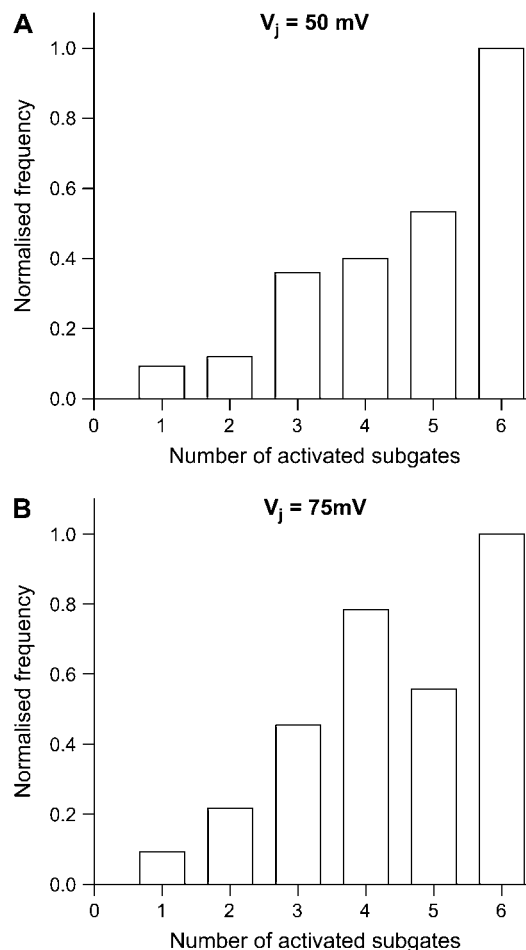

FIGURE 7 Dependence of substate frequency on number of subgates activated. The incidence of substate events was determined from current traces elicited by V_j pulses of 200-ms duration. The bar graphs show the relative frequency of events at different numbers of activated subgates, n. In each data set, the number of events at $n = 6$ was largest and hence was used for normalization. (*A*) Data at $V_j = 50$ mV (188 events from 235 pulses). (*B*) Data at $V_j = 75$ mV (301 events from 158 pulses).

resulting plot of dwell time versus number of activated subgates (five cell pairs). The symbols represent mean values $\pm$ 1 SE from 9–97 observations obtained at $V_j = 50$ mV (*solid circles*) and $V_j = 75$ mV (*open circles*). The graph reveals a positive correlation between subgate activation and dwell time for both data sets. Dwell times of substate 1 for $V_j = 50$ and 75 mV averaged 4.1 $\pm$ 0.5 and 3.0 $\pm$ 0.3 ms, respectively. In the case of substate 6, i.e., the residual state, they averaged 82 $\pm$ 7.3 and 96 $\pm$ 6.7 ms, respectively. Hence, the dwell time increased about 20- and 30-fold.

In fact, the residual state dwell time would be much longer since the residual state was forced to cease by the duration of the voltage pulse, which was evident when long V_j pulses (>1 s) were used. The triangles in Fig. 8 represent the results from 10 such current records at $V_j = 50$ mV (four cell pairs). It turned out that dwell times from long and short pulses were not distinguishable, except when six subgates were activated
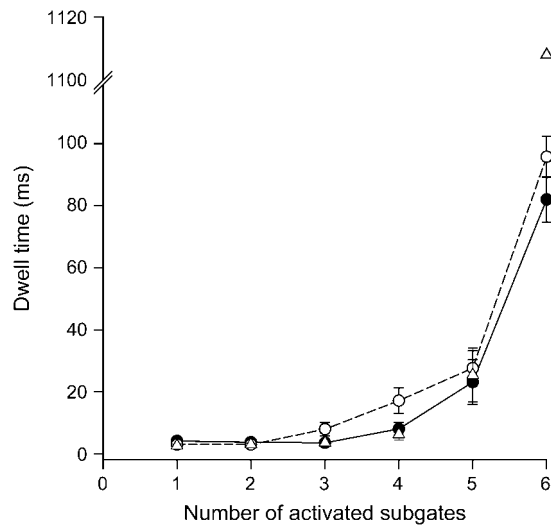
FIGURE 8 Relationship between duration of dwell times of substates and number of substates activated. Current traces were analyzed for dwell times of a channel at distinct substate levels. The dwell times were plotted as a function of the number of activated subgates. The symbols represent mean values ± 1 SE obtained at $V_j = 50$ mV (*solid circles, solid line*) and 75 mV (*open circles, dashed line*) using short voltage pulses (200 ms), and at $V_j = 50$ mV (*open triangles, no line*) using long voltage pulses (>1 s). Note the interruption of the y axis.

(corresponds to residual state). In this case, the respective dwell times were 1108 ± 528 ms as compared to 82 ± 7.3 ms in the case of short pulses at $V_j = 50$ mV.

Frequency of current transitions associated with substates

The data on substate events elicited by 200-ms voltage pulses were further analyzed examining the current transitions associated with channel substates. For this purpose, the transitions during each V_j pulse were counted and expressed as events per pulse. Records without any transitions (no subgate activated) were also included in the analysis provided they showed an activated channel (main state). The analysis yielded the following values: 0.89 ± 0.06 ($V_j = 50$ mV, 235 pulses), 2.12 ± 0.12 ($V_j = 75$ mV, 158 pulses), and 2.43 ± 0.15 ($V_j = 100$ mV, 76 pulses). These data correspond to 4.5, 10.6, and 12.2 transitions/s, respectively.

The bar graphs in Fig. 9 illustrate the normalized frequency of current traces with a given number of transitions per pulse, investigated at $V_j = 50$, 75, and 100 mV (panels A–C). The cases with one transition/pulse were used for normalization. A comparison of the graphs indicates that few transitions were more frequent than many transitions, irrespective of the voltage. The maximal number of transitions varied from 4 to 8, being largest at $V_j = 75$ mV. Moreover, the incidence of uneven transitions, which correspond to cases ending in substates, usually the residual state, was also largest at intermediate transjunctional voltage (43%, 65%,

and 59% for 50, 75, and 100 mV, respectively). Furthermore, the frequency of records without any transitions decreased with increasing V_j, decaying from 38 to 3 and 0% at $V_j = 50$, 75, and 100 mV, respectively.

Mathematical model

Several computer simulations were performed using the electrical schemes shown in Fig. 1 to study possible mechanisms of subgating. Fig. 10 shows plots of single-channel conductances, γ_j, versus transjunctional voltage, V_j, using different assumptions. In each plot, the top and bottom curve
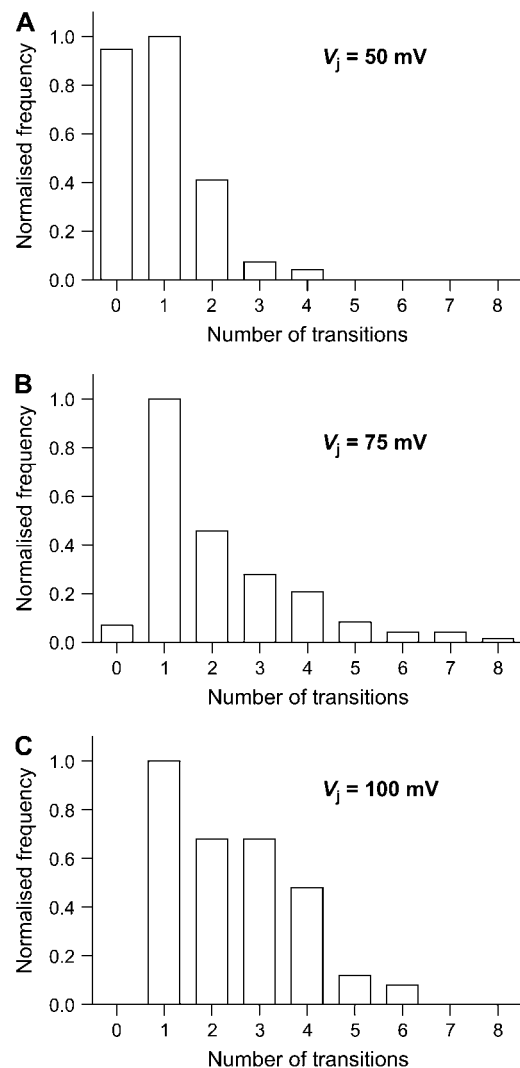

FIGURE 9 Histograms of current transitions. Current records elicited by V_j pulses of 200-ms duration were analyzed for the number of transitions associated with channel substates. The number of observations were plotted as a function of the number of transitions per current record. The case with one transition per record was used as reference for normalization. (A) Data at $V_j = 50$ mV: mean transitions/record = 0.89 ± 0.06 (235 pulses). (B) Data at $V_j = 75$ mV: 2.12 ± 0.12 (158 pulses). (C) Data at $V_j = 100$ mV: 2.43 ± 0.15 (76 pulses). Curves correspond to the best fit of data to an exponential (for interpretation, see text).
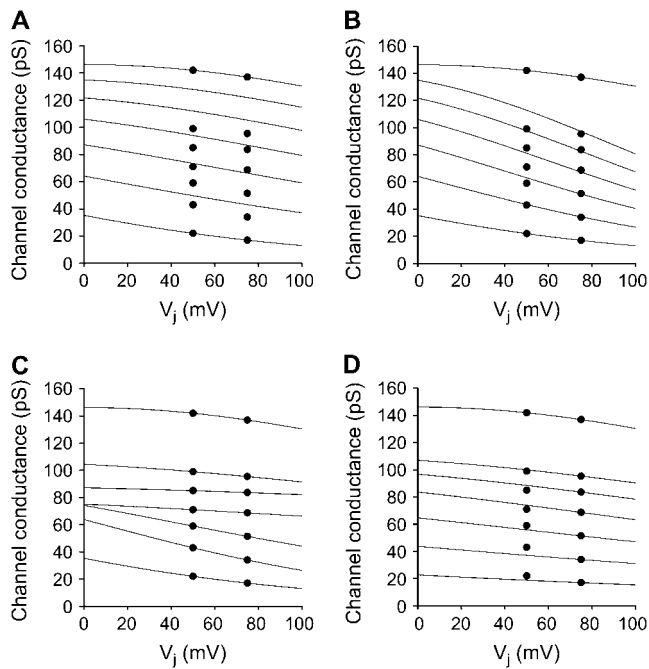
FIGURE 10 Comparison of biological data and computer simulations. (*A*) Independently working connexins. (*B*) Modification of *A* by setting the decay constants of substates 1–6 to V_L. (*C*) Individual fitting of every substate to the entire data set. (*D*) Individual fitting of every substate to the reduced data set measured at 75 mV. Graphs in *A* and *B* were calculated using the electrical scheme depicted in Fig. 1 *A*, graphs *C* and *D* using the scheme in Fig. 1 *B*, respectively. *Solid circles*, biological data; *continuous curves*, results of computer simulations.

correspond to the functions $\gamma_{j,\text{main state}}$ ($n = 0$) and $\gamma_{j,\text{residual state}}$ ($n = 6$), respectively.

In a first attempt to reproduce the conductive data of substates, main- and residual-state data of Cx30 channels were fitted to the generalized gap junction model (20,21). This procedure yielded the fitting parameters $\Gamma_H = 292.4$ pS, $V_H = -179.2$ mV, $\Gamma_L = 40.1$ pS, and $V_L = -88.5$ mV. These conductive parameters were then assigned to the connexins of each hemichannel according to Fig. 1 *A*. The resulting voltage-conductance curves are shown in Fig. 10 *A*. Obviously, there is no satisfying correlation between the model and the experimental data of substates 1–5 (from top to bottom).

For the second simulation, the degree of independence was limited by assigning identical decay constants to all connexins irrespective of the connexon conductive state, except for the substate $n = 0$, i.e., the main state. This was achieved by setting the decay constants to $V_L = -88.5$ mV while leaving unchanged the constant multiplier of the exponential functions. This approach corresponds to a hemichannel model with equally spaced constant multipliers between substates 0 and 6, and identical voltage sensitivities for the conductance of substates 1–6. The hemichannel is then described by a modification of Eq. 2:

$$\gamma_1 = \Gamma_H \times e^{V_{j1}/V_H} \tag{6}$$

$$\gamma_2 = \begin{cases} \Gamma_H \times e^{V_{j2}/V_H}, & n = 0 \\ \dfrac{(6-n) \times \Gamma_H + (n) \times \Gamma_L}{6} \times e^{V_{j2}/V_L}, & 1 \le n \le 6 \end{cases} \tag{7}$$

Fig. 10 *B* illustrates the result of this simulation, which demonstrates good agreement between experimental data and calculated conductances of substates 0, 4, 5, and 6. In contrast, calculated and experimental data of substates 1–3 match only for $V_j = 75$ mV.

The third simulation used the electrical scheme shown in Fig. 1 *B*. Each substate conductance was fitted to the appropriate data and the respective curves were plotted in Fig. 10 *C*. For the calculation, Γ_{sub0} and V_{sub0} of hemichannel cx_1 were set to $\Gamma_H = 292.4$ pS and $V_H = -179.2$ mV, i.e., hemichannel cx_2 toggles between substates. The resulting fitting parameters of cx_2 substates are summarized in Table 1. The large decay constants of cx_2 for substates 2–4 are caused by the small conductance variability between 50 and 75 mV.

The fourth simulation is a modification of the third by reducing the substate data set. The conductance data of $V_j = 50$ mV were not considered to calculate the fitting parameters. Fig. 10 *D* depicts the resulting conductance plot, which demonstrates good agreement between experimental and calculated data. Table 2 summarizes the fitting parameters and shows a clear pattern for the constant multiplier and the decay constants. For each subsequent substate, the constant multiplier alters between 24.1 and 34.1 pS and the substate decay constants vary in a narrow range between -201.8 and -233.6 mV, i.e., within 14%.

DISCUSSION

Transfected HeLa cells expressing mouse Cx30 turned out to be suitable to explore the properties of substates of gap junction channels in a quantitative manner. Examining single-channel currents in preformed cell pairs, we found several

TABLE 1 Parameters used for fitting substates to the entire data set in comparison of biological data with computer simulations

Substate	cx_2	
	Γ_0 (pS)	V_0 (mV)
0	292.4	−179.2
1	162.4	−280.4
2	124.2	−564.4
3	101.1	−407.6
4	99.5	−130.2
5	81.5	−88.1
6	40.1	−88.5

The parameters used are those represented in Fig. 10 *C*. The parameters of hemichannel cx_1 were derived from substate 0, i.e., the main state, and were kept constant for the calculation of the parameters of cx_2.

TABLE 2 Parameters used for fitting substates to the reduced data set in comparison of biological data with computer simulations

Substate	Γ_0 (pS)	V_0 (mV)	$\Gamma_{0(n)} - \Gamma_{0(n-1)}$ (pS)
		cx_2	
0	292.4	−179.2	—
1	168.7	−233.6	−123.7
2	144.6	−221.7	−24.1
3	117.1	−201.8	−27.5
4	83.0	−208.6	−34.1
5	51.4	−226.0	−31.6
6	24.6	−226.5	−26.8

The parameters used are those represented in Fig. 10 *D*. The parameters of hemichannel cx_1 are derived from substate 0, i.e., the main state, and were kept constant for the calculation of the other substates.

discrete levels elicited by transjunctional voltage, V_j. Between the already established main state and residual state (19), we identified five additional levels attributable to channel substates. Moreover, we have adapted our mathematical gap junction model (20,21) to include channel substates. The expanded model was used to simulate the channel properties and analyze the data from the biological experiments.

In the presence of appropriate V_j gradients, I_j mainly flickered between two discrete levels, giving rise to the conductances $\gamma_{j,main\ state}$ and $\gamma_{j,residual\ state}$, indicating that the channels do not close completely. Between these two prominent events, the signals often showed additional current levels of short duration. Since the extra events were present in single-channel records, they reflect substates and not main states or residual states of other channels. Hence, their conductances were designated $\gamma_{j,substate}$. The analysis of unitary current records yielded conductance histograms with six distinct peaks (see Fig. 3). This is consistent with the view that each connexin of a hemichannel acts as a voltage-sensitive subgate (14,15). Hence, the main state and residual state represent conditions with all subgates inactivated or activated, respectively, whereas the five substates in between correspond to the situation with from 1 to 5 subgates activated. This concept is compatible with the structure of gap junction channels. It confines the structure of voltage gating to the six connexins of connexons cx_1 or cx_2, depending on the polarity of V_j. Cx30 gap junction channels are thought to gate with positive voltage (17, but see also 28).

Conductance properties of substates

To emphasize the changes in channel conductance, the amplitude of the current steps observed was determined using $I_{j,main\ state}$ as reference level, i.e., $\Delta I_j = I_{j,main\ state} - I_{j,substate}$. The signals analyzed in this way revealed conductance histograms with six discrete conductances. These data were then used to explore the relationship between the conductance steps of channel substates, $\Delta\gamma_j$, and the number

of subgates activated, n (see Fig. 4). It turned out that the function $\Delta\gamma_j = f(n)$ was slightly curved for the data at $V_j = 50$ mV (*solid circles*) and 75 mV (*open circles*). The conductance steps became progressively larger with the number of activated subgates. Given that both hemichannels exhibit voltage-dependent conductances (for $\gamma_{j,main\ state}$ and $\gamma_{j,residual\ state}$ of Cx30, seeValiunas et al. (19); for our model, see Vogel and Weingart (20,21)), this finding can be interpreted as follows. Provided that a gap junction channel changes its state, i.e., its conductance, the voltage drops across the hemichannels cx_1 and cx_2 are redistributed, which in turn leads to new conductances of cx_1 and cx_2. With regard to substates, incremental activation of subgates in the gating hemichannel (e.g., cx_1) gradually reduces its conductance and, concomitantly, reduces the voltage drop across the nongating hemichannel (i.e., cx_2). As a result, the conductance of cx_2 converges to the value of Γ_H (20) and the conductance of the gap junction channel becomes progressively more dominated by the properties of cx_1.

To convert conductance levels into channel conductances prevailing at different subgate conditions, the $\Delta\gamma_j$ data were reexpressed as $\gamma_j = \gamma_{j,main\ state} - \Delta\gamma_j$ and plotted versus number of subgates activated (see Fig. 5). The graphs indicate that the channel conductance levels are not equally spaced between the main state, i.e., $n = 0$, and the residual state, i.e., $n = 6$. Activation of the first subgate produced by far the largest conductance change (~30%), whereas successive activation of remaining subgates gave rise to small changes of increasing size. The role of the first subgate on channel property is even more dramatic when the calculated conductances of a gated hemichannel are considered. As shown in Fig. 6, the relationship $\gamma_{j,cx}$ versus number of activated subgates exhibits a sharp break at $n = 1$, thus leading to a steep decline between $n = 0$ and $n = 1$ (~47%) and a shallow decline between $n = 1$ and $n = 6$. Hence, in a gap junction channel, the nongating hemichannel attenuates the dramatic conductance change accompanied by the activation of the first subgate of the gating hemichannel.

Overall, the conductance data at $V_j = 50$ mV were slightly larger than those at $V_j = 75$ mV, irrespective of the number of subgates involved (see Figs. 5 and 6). For example, in the case of hemichannels, the conductances $\gamma_{hc,main\ state}$ and $\gamma_{hc,residual\ state}$ were 284/274 pS and 24/18 pS for V_j at 50/75 mV, respectively. This is consistent with the moderate voltage sensitivity of the single-channel functions $\gamma_{j,main\ state} = f(V_j)$ and $\gamma_{j,residual\ state} = f(V_j)$, which translates into the voltage sensitivity of the multichannel functions $g_{j,inst} = f(V_j)$ at large and small voltages, and $g_{j,ss} = f(V_j)$ at large voltages, respectively (19).

Simulations and biologic implications

Computer simulations were made to elucidate the results obtained from the biological experiments. For this purpose, our generalized gap junction model was expanded to

incorporate substates (see Fig. 1). Several attempts were made to simulate the conductive behavior of these states (see Fig. 10). In these presentations, the biological data gathered are represented by two columns at $V_j = 50$ and 75 mV, respectively. The simulations indicate that channel conductances are strongly sensitive to V_j for each substate condition.

The first simulation (see Fig. 10 A) describes the experimental data inadequately. Hence, the underlying model, which assumed independently working connexins, has to be discarded. The second simulation (see Fig. 10 B), based on restricted independency of connexin function, reproduced the biological data more satisfactorily. The third simulation (see Fig. 10 C), i.e., the fitting to experimental data, assumed that the nongating hemichannel remains in its high conductance state. It demonstrated grouping of conductance curves and parameters of substates 1–3 as well as substates 4–6. This finding further underscores the functional interdependence of the connexins from the gating hemichannel.

In the case of the second and fourth simulation (see Fig. 10, B and D), the data at $V_j = 75$ mV are in good agreement with the simulations. However, in both cases there is some misfit for data at $V_j = 50$ mV. For example, in Fig. 10 B, the data for $n = 4$–6 are in accord, whereas simulated conductances of substates 1–3 overestimate the biological data; in Fig. 10 D, the data for $n = 1$–3 are slightly too small, those for $n = 4$–6 slightly too large. The discrepancies at $V_j = 50$ mV may be explained as follows. Due to a larger signal/noise ratio, the data at $V_j = 75$ mV may be more accurate than those at $V_j = 50$ mV. Moreover, errors due to tip potentials are expected to be larger at smaller V_j. Hence, it may be justified to weight data at $V_j = 75$ mV more than those at $V_j = 50$ mV.

Summarized, the simulations emphasize the following conclusions with regard to the underlying mechanisms of substate conductance behavior. Nonlinear hemichannel voltage-conductance relationships (17,20) cause an uneven distribution of substate conductance levels interposed between the main and residual state. This distribution is modified by the presence or absence of functionally interdependent connexins. However, the comparison with biologic data favors a model with interdependent connexin function as shown in Fig. 10 D and Table 2.

The following molecular scheme could accommodate these observations. The conductance decay upon subgate recruitment may reflect two processes. First, narrowing of the hemichannel pore, presumably caused by conformational changes of the transmembrane segments of its connexins. The conformational change of a connexin, i.e., the spatial redistribution of its charges, is expected to influence the conformation of the other connexins from a hemichannel and thus may explain the interdependency of connexin function as reflected by the similar decay constants, V_o, of the subgates and the residual state (see Table 2). Second, partial blocking of the hemichannel pore brought about by dislocation of the C-terminal domain of its connexins, analogous to the ball-

and-chain model (29), which may be consistent with the quite even reduction of parameter Γ_o between following substates (see Table 2). Hence, narrowing of the pore is a prerequisite for partial blocking of the pore; the former may contribute ~40% to the conductance change, the latter 10%.

Kinetic properties of substates

Current levels emanating from subgates were infrequent and short-lasting. This rendered quantitative studies difficult, especially the analysis of kinetic properties. Nonetheless, inspecting the time domain of current records permitted qualitative insight.

Current transitions associated with substates were fast, elapsing within the response time of the experimental set-up (1–2 ms). Hence, they resemble those seen during flickering between the main state and residual state (19). In most cases, substates started with a fast current transition from the channel main state and ended with a fast transition back to the main state, irrespective of the substate level reached. Hence, substates follow an activation pattern with the channel main state as the initial state. Current transitions between substates were virtually absent, transitions from a substate to the residual state were rare, i.e., 2–3% of all events. This pattern of activation and inactivation suggests that channel substate levels are not occupied in a random fashion. Subgates seem to be operated concurrently rather than sequentially.

In absolute terms, the channel substates were available more frequently at larger voltage. Hence, the contribution of substate events to I_j inactivation increases with increasing amplitude of V_j. In relative terms, substates with more activated subgates occurred more often, irrespective of V_j. Hence, subgates activate and inactivate mostly in groups and rarely alone, suggesting a high degree of cooperativity. Voltage appeared to have no effect on the distribution of the relative incidence of substates. However, it cannot be excluded that this reflects the narrow voltage range explored.

The dwell time of channel substates was variable, ranging from about 3 to 90 ms for 200-ms pulses. The duration of dwell time increased with increasing number of subgates activated (see Fig. 8). At channel state $n = 6$, the dwell times lasted about 20-fold ($V_j = 50$ mV) and 30-fold ($V_j = 75$ mV) longer than at state $n = 1$. The positive correlation between dwell time and number of activated subgates facilitates I_j inactivation via both an increase in dwell time duration and recruitment of several subgates. Moreover, the small V_j sensitivity of this correlation indicates that dwell times tend to prolong with increasing voltage. In the case of $V_j = 50$ mV, dwell times were also determined with long voltage pulses (>1 s). Under this condition, the dwell-time duration of substates 1–5 was comparable to those found with 200-ms pulses (see Fig. 8). However, for substate 6, it was about 13-fold longer. Hence, substates 1–5 occur mainly early during V_j pulses and substate 6 mainly late during V_j pulses.

This accentuates the role of the residual states for inactivation of I_j in the case of long pulses.

Currents elicited by 200-ms pulses were also analyzed to evaluate the number of transitions. It turned out that the transitions/s increased from 4.5 to 10.6 and 12.2 for $V_j = 50$, 75, and 100 mV, respectively. Hence, the incidence of transitions increased with increasing V_j. Moreover, the analysis revealed that current records with few transitions were more frequent than those with many transitions (see Fig. 9). Furthermore, there was a distinct shift from pulses with no or few transitions to pulses with several transitions when V_j was increased from 50 to 100 mV. Hence, an increase in voltage may enhance I_j inactivation via an increase in the number of transitions.

The limited response time of the experimental setup (1–2 ms) may have prevented the detection of very short-lived substates. This would affect the kinetic data presented, notably the frequency and duration of substates. Moreover, it would question the conclusion that subgates are operated concurrently (see above). In the cell-pair approach used, the patch pipettes are not in direct contact with the gap junction channels. This prevents a very rapid voltage control, thus limiting the frequency response of the setup.

Functional relevance of substates

If one assumes that gap junction channels are open under physiological conditions, substates may be regarded as failed attempts to transit from main state to residual state during I_j inactivation and from residual state to main state during I_j restitution. Hence, they are expected to slow down the kinetics of I_j associated with voltage gating. This should result in an extra time constant of I_j changes. However, examining multichannel currents carried by Cx30 channels, we found that I_j inactivation proceeds with a single time constant (19). This is a surprise, given the significant substate activity of these channels. An explanation may be that the contribution of substates was negligible or that the time constants were similar and hence could not be distinguished. Interestingly, other gap junction channels have been reported to show two time constants of I_j inactivation and restitution (e.g., Cx45 (30), Cx43 (31), or Cx46 (11)). Conceivably, substates may contribute in these cases. However, an alternative explanation may be that slow gating of gap junction channels contributes to the extra time constant (32,33).

Substates may also play a role as selectivity and permeability filter of gap junction channels (34). Common molecular coupling may turn into restricted molecular coupling or even give way to selective ionic coupling. Combined quantitative electrical and diffusional studies will have to elucidate the underlying mechanisms.

REFERENCES

1. Unger, V. M., N. M. Kumar, N. B. Gilula, and M. Yeager. 1999. Three-dimensional structure of a recombinant gap junction membrane channel. *Science*. 283:1176–1180.

2. Willecke, K., J. Eiberger, J. Degen, D. Eckhardt, A. Romualdi, M. Güldenagel, J. Deutsch, and G. Söhl. 2002. Structural and functional diversity of connexin genes in the mouse and human genome. *J. Biol. Chem.* 383:725–737.

3. Somogyi, R., and H.-A. Kolb. 1988. Cell-to-cell channel conductance during loss of gap junctional coupling in pairs of pancreatic acinar and Chinese hamster ovary cells. *Pflugers Arch.* 412:54–65.

4. Chen, Y. H., and R. L. De Haan. 1992. Multiple channel conductance states and voltage regulation of embryonic chick cardiac gap junctions. *J. Membr. Biol.* 127:95–111.

5. Perez-Armendariz, E. M., M. C. Romano, J. Luna, C. Miranda, M. V. L. Bennett, and A. P. Moreno. 1994. Characterization of gap junctions between pairs of Leydig cells from mouse testis. *Am. J. Physiol.* 267:C570–C580.

6. Veenstra, R. D., H. Z. Wang, E. C. Beyer, S. V. Ramanan, and P. R. Brink. 1994. Connexin37 forms high conductance gap junction channels with subconductance state activity and selective dye and ionic permeabilities. *Biophys. J.* 66:1915–1928.

7. Bukauskas, F. F., C. Elfgang, K. Willecke, and R. Weingart. 1995. Biophysical properties of gap junction channels formed by mouse connexin40 in induced cell pairs of transfected human HeLa cells. *Biophys. J.* 68:2289–2298.

8. Valiunas, V., F. F. Bukauskas, and R. Weingart. 1997. Conductances and selective permeability of connexin43 gap junction channels examined in neonatal rat heart cells. *Circ. Res.* 80:708–719.

9. Oh, S., J. B. Rubin, M. V. L. Bennett, V. K. Verselis, and T. A. Bargiello. 1999. Molecular determinants of electrical rectification of single channel conductance in gap junctions formed by connexins 26 and 32. *J. Gen. Physiol.* 114:339–364.

10. Hopperstad, M. G., M. Srinivas, and D. C. Spray. 2000. Properties of gap junction channels formed by Cx46 alone and in combination with Cx50. *Biophys. J.* 79:1954–1966.

11. Sakai, R., C. Elfgang, R. Vogel, K. Willecke, and R. Weingart. 2003. The electrical behaviour of rat connexin46 gap junction channels expressed in transfected HeLa cells. *Pflugers Arch.* 446:714–727.

12. Churchill, D., and S. Caveney. 1993. Double whole-cell patch-clamp characterization of gap junctional channels in isolated insect epidermal cell pairs. *J. Membr. Biol.* 135:165–180.

13. Ramanan, S. V., and P. R. Brink. 1993. Multichannel recordings from membranes which contain gap junctions. II. Substates and conductance shifts. *Biophys. J.* 65:1387–1395.

14. Bukauskas, F. F., and R. Weingart. 1993. Multiple conductance states of newly formed single gap junction channels between insect cells. *Pflugers Arch.* 423:152–154.

15. Bukauskas, F. F., and R. Weingart. 1994. Voltage-dependent gating of single gap junction channels in an insect cell line. *Biophys. J.* 67:613–625.

16. Trexler, E. B., M. V. L. Bennett, T. A. Bargiello, and V. K. Verselis. 1996. Voltage gating and permeation in a gap junction hemichannel. *Proc. Natl. Acad. Sci. USA*. 93:5836–5841.

17. Valiunas, V., and R. Weingart. 2000. Electrical properties of gap junction hemichannels identified in transfected HeLa cells. *Pflugers Arch.* 440:366–379.

18. Christ, G. J., and P. R. Brink. 1999. Analysis of the presence and physiological relevance of subconducting states of connexin43-derived gap junction channels in cultured human corporal vascular smooth muscle cells. *Circ. Res.* 84:797–803.

19. Valiunas, V., D. Manthey, R. Vogel, K. Willecke, and R. Weingart. 1999. Biophysical properties of mouse connexin30 gap junction channels studied in transfected human HeLa cells. *J. Physiol.* 519:631–644.

20. Vogel, R., and R. Weingart. 1997. Mathematical model of vertebrate gap junctions derived from electrical measurements on homotypic and heterotypic channels. *J. Physiol.* 510:177–189.

21. Vogel, R., and R. Weingart. 2002. The electrophysiology of gap junctions and gap junction channels and their mathematical modelling. *Biol. Cell.* 94:501–510.

22. Valiunas, V., D. Manthey, K. Willecke, and R. Weingart. 1996. Electrical properties of connexin30 gap junction channels studied in transfected HeLa cells. *Pflugers Arch.* 431(Suppl):R93.

23. Weingart, R., V. Valiunas, K. Willecke, and D. Manthey. 1996. Electrical properties of Cx30 gap junction channels studied in transfected HeLa cells. *Keystone Conference: Molecular Aspects to the Function of Intercellular Junctions*, Lake Tahoe, CA. 43 pp.

24. Dahl, E., D. Manthey, Y. Chen, H.-J. Schwartz, Y. S. Chang, P. A. Lalley, B. C. Nicholson, and K. Willecke. 1996. Molecular cloning and functional expression of mouse connexin-30, a gap junction gene highly expressed in adult brain and skin. *J. Biol. Chem.* 271: 17903–17910.

25. Krisciukaitis, A. 1997. Computer programs for investigation of intercellular communication using double whole-cell voltage clamp. *Electron. Elect. Eng.* (Lithuania) 4:71–83.

26. Schmilinsky-Fluri, G., V. Valiunas, M. Willi, and R. Weingart. 1997. Modulation of cardiac gap junctions: The mode of action of arachidonic acid. *J. Mol. Cell. Cardiol.* 29:1703–1713.

27. Kullmann, D. M. 1989. Application of the expectation-maximization algorithm to quantal analysis of postsynaptic potentials. *J. Neurosci. Methods.* 30:231–245.

28. Harris, A. L. 2001. Emerging issues of connexin channels: biophysics fills the gap. *Q. Rev. Biophys.* 34:325–472.

29. Zagotta, W. N., T. Hoshi, and R. W. Aldrich. 1990. Restoration of inactivation in mutants of *Shaker* potassium channels by a peptide derived from ShB. *Science.* 250:568–571.

30. Barrio, L. C., J. Capel, J. A. Jarillo, C. Castro, and A. Revilla. 1997. Species-specific voltage-gating properties of connexin-45 junctions expressed in *Xenopus* oocytes. *Biophys. J.* 73:757–769.

31. Valiunas, V., R. Vogel, and R. Weingart. 2000. The kinetics of gap junction currents are sensitive to the ionic composition of the pipette solution. *Pflugers Arch.* 440:835–842.

32. Banach, K., and R. Weingart. 2000. Voltage gating of Cx43 gap junction channels involves fast and slow current transitions. *Pflugers Arch.* 439:248–250.

33. Bukauskas, F. F., A. B. Angele, V. K. Verselis, and M. V. L. Bennett. 2002. Coupling asymmetry of heterotypic connexin 45/connexin 43-EGFP gap junctions: properties of fast and slow gating mechanisms. *Proc. Natl. Acad. Sci. USA.* 99:7113–7118.

34. Qu, Y., and G. Dahl. 2002. Function of the voltage gate of gap junction channels: selective exclusion of molecules. *Proc. Natl. Acad. Sci. USA.* 99:697–702.